THE JOURNAL OF PHYSICAL CHEMISTRY C

Article

pubs.acs.org/JPCC

Relation between Distortions in the Oxygen Sublattice and the Local Order of Zr in Nanostructured ZrO_2–CeO_2 Mixed Oxides

Leandro M. Acuña,*[,†,⊥] Rodolfo O. Fuentes,[‡,⊥] Marcia C. A. Fantini,[§] and Diego G. Lamas[∥,⊥]

[†]DEINSO (Depto. de Investigaciones en Sólidos), CITEDEF, J.B. de La Salle 4397, 1603 Villa Martelli, Buenos Aires, Argentina

[‡]Departamento de Física, Centro Atómico Constituyentes, CNEA, Av. Gral. Paz 1499, 1650 San Martín, Buenos Aires, Argentina

[§]Instituto de Física, Universidade de São Paulo, Travessa R da Rua do Matão, no.187, Cidade Universitária, 05508-090, São Paulo, Brazil

[∥]Laboratorio de Caracterización de Materiales, Facultad de Ingeniería, Universidad Nacional del Comahue, Buenos Aires 1400, 8300 Neuquén, Pcia. de Neuquén, Argentina

[⊥]CONICET, Av. Rivadavia 1917, 1033 Buenos Aires, Argentina

ABSTRACT: In the present work, the local order of Zr in ZrO_2–CeO_2 nanopowders (with 50, 65, 70, and 90 mol % CeO_2) was studied by extended X-ray absorption fine structure around the Zr K-edge. In the cases of ZrO_2–50 and 65 mol % CeO_2, we studied how the local order is affected by the phase transition at high temperature. In order to study the tetragonal-cubic phase transition as a function of temperature, high-temperature synchrotron radiation X-ray powder diffraction (SR-XPD) was employed. We explored different models of the local atomic structure and interpreted them as distortions of the accepted long-range order deduced by XPD analyses. The results suggested the existence of distortions in the oxygen sublattice, which can be accounted for as displacements of the oxygen atoms along the (110) direction of the pseudofluorite unit cell that cannot be observed by XPD because of the random nature of these displacements.

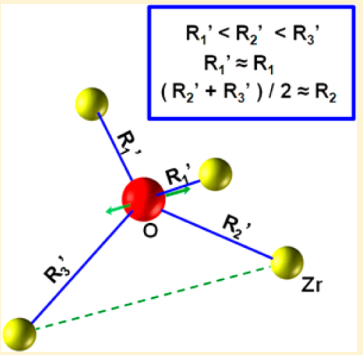

INTRODUCTION

ZrO_2–CeO_2 substitutional solid solutions have attracted particular interest in recent years due to their extensive use in different fields, for example, as active supports or "oxygen buffers" in three-way catalysts (which are applied in controlling the emissions of NO_x, CO, and hydrocarbons from automotive exhausts). The properties of zirconia–ceria mixed oxides are strongly related to their crystal structure. In particular, the metastable forms of the tetragonal phase have been widely investigated since they are the most suitable for some applications. This wide use of these systems as catalyst components prompted a renewed interest with regards to these materials in the form of nanosized, high surface area powders. In particular, in the catalytic converter, CeO_2 is presented as a mixed oxide with ZrO_2. Without the addition of zirconia, ceria sinters rapidly in high-temperature applications, losing surface area and catalytic activity. In contrast, CeO_2–ZrO_2 mixtures maintain their surface area and catalytic activity for many years under very harsh environments. Such thermal stability would be advantageous in catalysts for applications in SOFC-related catalyst systems.[1,2]

Pure ZrO_2 exhibits three different phases with increasing temperature under normal atmospheric pressure. From room temperature to 1130 °C, the monoclinic phase (m, $P2_1/c$ space group) is the stable one. Between 1130 and 2370 °C, it exhibits the tetragonal phase (t, $P4_2/nmc$). For temperatures higher than 2370 °C, it transforms to the cubic phase (c, $Fm\bar{3}m$), which also has a fluorite structure. These high-temperature phases, t and c, exhibit the best properties for technological applications and can be retained at room temperature in metastable form by doping with di-, tri-, or tetra-valent cations. In particular, for Ce^{4+} cations, compositionally homogeneous ZrO_2–CeO_2 solid solutions were obtained in a wide composition range.[3−14] In the case of the tetragonal phase, two forms, t' and t'', were found, which differentiate in the axial ratio c/a. The t'' form exhibits $c/a = 1$, whereas $c/a > 1$ for the t' one. In both cases, oxygen atoms are displaced along the c axis from the ideal site in the fluorite unit cell, and this feature differentiates the tetragonal forms from the cubic phase. As a consequence of the oxygen displacement, the X-ray powder diffraction (XPD) pattern exhibits a very weak reflection along the (112) direction of the pseudofluorite unit cell, which is forbidden in the cubic phase but allowed in the tetragonal phase. Neutron diffraction is a more suitable technique for the (112) detection, due to the bigger scattering cross section that the oxygen atom exhibits to neutron radiation with respect to X-ray photons. For example, Yashima et al. have published several works related to the t–c phase transition of the ZrO_2–CeO_2 system using neutron diffraction.[7,8] However, our previous studies on ZrO_2-based solid solutions by synchrotron XPD demonstrated that this weak reflection can be accurately

Received: March 11, 2014
Revised: April 10, 2014
Published: May 5, 2014

studied by using a synchrotron X-ray source and a high-intensity configuration.[11,12]

The local structure of ZrO_2−CeO_2 (ZC) powders has been extensively studied, and some main features have been determined. One important result is that the first oxygen shell around Ce has the characteristics expected for pure CeO_2 (fluorite-type crystal structure, one shell with 8 oxygen atoms) regardless of if the crystalline phase is *t* (*t*′, *t*″ forms) or *c*, which is totally unexpected for a substitutional solid solution, from a crystallographic point of view.[8,15] In contrast, the first shell around Zr atoms exhibits differences related to the changes in the crystal structure. This means that it splits into two oxygen subshells for the tetragonal forms (as expected according their crystal structure) and exhibits only one shell for the *c* phase. In other words, the tetragonal-to-cubic phase transition is related to a symmetry change of the oxygen first shell around Zr atoms, whereas that around Ce atoms remains unaltered.[15]

Despite these general features of the local order of ZC solid solutions, there is no general consensus in some other aspects, particularly regarding the detailed features of the first oxygen shell around the Zr atom. Several authors have reported that Zr is coordinated with six or seven nearest-neighbor oxygen atoms in the first coordination shell, while the expected coordination (from crystal structure) for the *t* and *c* phases is eight.[12,16,17] In the case of the *c* phase, there is only one Zr−O distance. On the other hand, in the *t* phase, there are two Zr−O distances, each subshell with four oxygen atoms, as a consequence of the O displacement along the *c* axis. Other authors proposed a model that does not consider the existence of vacancies, consisting of two subshells with four atoms in each one, but with different Debye−Waller factors (σ^2, in Å^2), which gives a measure of the disorder or deviation from a calculated Zr−ion distance (*R*) for a given coordination shell or subshell.[18−20] Nevertheless, different σ^2 values for subshells that correspond to the same crystallographic sites (4*c* of the $P4_2/nmc$ space group) is unacceptable from the crystallographic point of view. Therefore, the key question in this discussion is how to interpret the local order of Zr in a ZrO_2−CeO_2 system, taking into account that it cannot be described by the crystallographic *t*- or *c*-models.

Previous studies demonstrated, that diminishing the average crystallite size to the nanoscale, the tetragonal-to-cubic phase transition temperature decreases for a given Ce content in a zirconia−ceria system.[12] This fact indicates that the phase diagram depends on the average size of the crystals, and important changes can be found when reducing the characteristic size down to the nanometer range.

This work deals with the study of the structural properties of ZrO_2−CeO_2nanopowders (of different compositions) and the local order of Zr in these nanopowders by means of extended X-ray absorption fine structure (EXAFS). In the cases of ZrO_2−50 and 65 mol % CeO_2, we studied how the local order is affected by the phase transition at high temperature. We explored different models and interpreted them as distortions of the accepted long-range order deduced by XPD analyses. The results of this study give some insight of the possible distortions that undergo in the oxygen sublattice that cannot be seen by XPD analyses and can help us to understand the underlying mechanisms that make possible the retention of the high-temperature phases of the nanostructured ZrO_2−CeO_2 system at room temperature in metastable form.

EXPERIMENTAL SECTION

Nanostructured, compositionally homogeneous ZrO_2−CeO_2 solid solutions were synthesized by a pH-controlled nitrate−glycine gel-combustion method (GC).[10−12] $ZrOCl_2·8H_2O$ (99.9%, Alpha Aesar, Ward Hill, Massachusetts) and $Ce(NO_3)_3·6H_2O$ (99.9%, Alpha Aesar, Ward Hill, Massachusetts) were dissolved in 50 mL of nitric acid (65%, Merck, Darmstadt, Germany) in an appropriate ratio in order to obtain ZrO_2−50, 65, 70, and 90 mol % CeO_2. These solutions were concentrated by thermal evaporation in order to eliminate chloride anions. Glycine (99%, Merk, Darmstadt, Germany) was added in a proportion of 5 mol/mol of metal atom, and the pH of the solution was adjusted to 7. The resulting solution was concentrated using a hot plate at 200 °C to get the homogeneous gel, which was further heated until a vigorous exothermic reaction started. The combustion product was then calcined in air at 600 °C for 2 h for carbon removal. The nomenclature used in this paper will be ZC50, ZC65, ZC70, and ZC90.

Structural properties at different temperatures in static air were studied by synchrotron radiation X-ray powder diffraction (SR-XPD) in the D10B-XPD beamline of the LNLS (Brazilian Synchrotron Light Laboratory, Campinas, Brazil). In order to detect the rather weak (112) reflection, a high-intensity (low-resolution) configuration, without crystal analyzer, was employed.[21] The wavelength λ was set to 1.5496 Å (8 keV) using a Si(111) monochromator. Data corresponding to ZC50 and ZC65 were collected between room temperature and 850 °C, in order to study the phase transitions $t' \rightarrow c$ and $t'' \rightarrow c$. At room temperature, the complete SR-XPD pattern was collected between 2θ = 20° and 85° with a 2θ step of 0.05° and a step counting time of 2 s. For higher temperatures, selected regions were measured, corresponding to the (111), (112), and (400) reflections of the pseudofluorite unit cell. The 2θ interval of 40−44°, corresponding to the (112) reflection, was measured with a longer counting time of 15 s in order to achieve a good signal-to-noise ratio. The other samples were measured only at room temperature, since the (112) reflection is very difficult to detect for ZC70, and the cubic phase (the (112) reflection is forbidden) is expected for ZC90.

The O displacement along the *c* axis can be calculated from the integrated intensities ratio of the (111) and (112) reflections. For the synchrotron radiation source and Bragg−Brentano geometry, they satisfy the following relation

$$\frac{I(112)}{I(111)} = \frac{4f_O^2 \sin^2(4\pi z(O)) q_O^2 L_{112}}{f_{Zr-Ce}^2 q_{Zr-Ce}^2 L_{111}} \quad (1)$$

where f_O^2 is the atomic form factor of the O^{2-} anion, q_O^2 its temperature factor, z(O) the fractional coordinate of O^{2-} in the asymmetric unit of the tetragonal unit cell, f_{Zr-Ce}^2 the atomic form factor of Zr^{4+} and Ce^{4+}cations, and q_{Zr-Ce}^2 the average temperature factor. On the other hand, the average crystallite size *D* was calculated using Scherrer's formula, $D = 0.9\lambda/(B·\cos\theta_{111})$, were *B* is the full width at half-maximum (fwhm) of the deconvoluted (111) Bragg peak.

EXAFS measurements of the Zr K-edge (17998 eV) were carried out at the D04B-XAFS1 beamline of the LNLS.[22] Energy was selected using a Si(111) double-crystal monochromator. Spectra were collected in transmission mode between 17 800 and 18 900 eV with an energy step of 2 eV and a step counting time between 8 and 12 s, in the temperature range of 20−600 °C. Two or four scans were

dx.doi.org/10.1021/jp502457w | J. Phys. Chem. C 2014, 118, 11445−11453

measured and averaged in order to improve the signal-to-noise ratio. The samples were prepared as a mixture of the powder to be studied and boron nitride (BN) and then pressed (2 ton/cm^2) into pellets of 13 mm in diameter.

EXAFS data reduction was done using WINXAS 3.1 code.[23] Absorption edge energy E_0 was taken as the absolute maximum of the first derivative dμ/dE (≈18 012 eV). Theoretical phases and amplitudes of the single scattering paths were calculated using ATOMS and FEFF8.2 codes.[24,25] Fittings were carried out using FEFFIT code.[26] The Fourier transforms (FTs) were calculated on the k^3-weighted EXAFS signal, $\chi(k)$, in the wavenumber range of k = 2.3−13.0 Å^{-1} employing a Gaussian window. Fittings were performed in the R-space in the range of R = 1.4−4.0 Å, which includes Zr−O (1st coordination shell), Zr−Zr and Zr−Ce (2nd coordination shell), and Zr−O (3rd coordination shell) single-scattering paths contributions. Multiple-scattering paths turned out to have negligible contribution to the fitting function. Tables 3, 4, and 5 show detailed specifications about the local order models considered in this study.

RESULTS AND DISCUSSION

SR-XPD patterns collected at room temperature and corresponding to ZC50, ZC65, ZC70, and ZC90 nanopowders are exhibited in Figure 1. The average crystallite size was

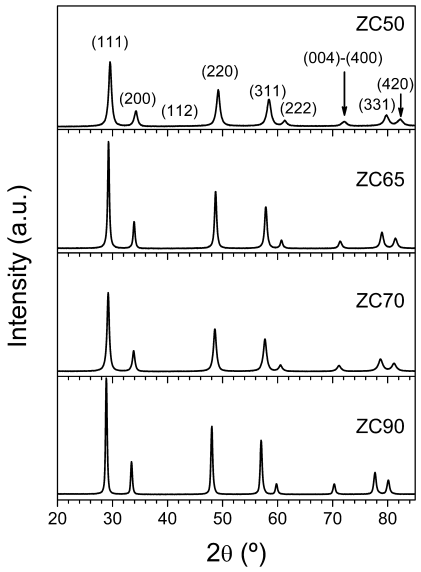

Figure 1. Room-temperature SR-XPD patterns of nanostructured ZC50, ZC65, ZC70, and ZC90 solid solutions. Main reflection peaks are indicated in the top panel.

12.0(6), 35.2(4), 22.0(4), and 38.3(3) nm, respectively. It is worth to mention that D was kept constant in the whole analyzed temperature range. Figure 2 shows a comparison of the peak located between 2θ = 69° and 74° due to the reflection along the (400) and (004) directions and corresponding to ZC50, ZC65, and ZC70 samples at room temperature. The main difference between ZC50 and the other two samples is that the former exhibits the typical (004)−(400) splitting (as an asymmetry at lower angles) of the t' form due to the axial relation $c > a$, while this peak is symmetrical in ZC65 and ZC70, indicating that the t'' form or c phase is present. Shifts in the peak position to lower angles with increasing Ce

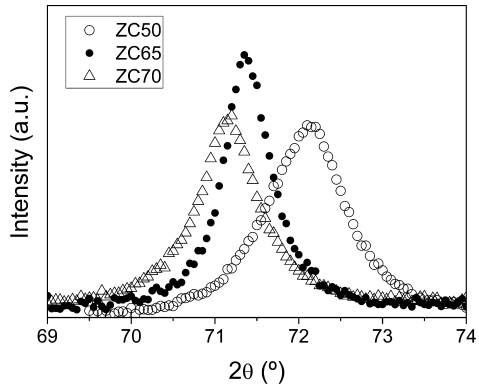

Figure 2. Room-temperature SR-XPD patterns in the vicinity of the (004) and (400) peaks for nanostructured ZC50, ZC65, and ZC70 solid solutions.

content is expected due to the larger ionic radius of Ce^{4+} with respect to that of Zr^{4+}.

To distinguish the t'' form from the c phase, it is necessary to analyze the 40° < 2θ < 44° region of the XPD pattern to observe whether or not the (112) reflection is present. Figure 3

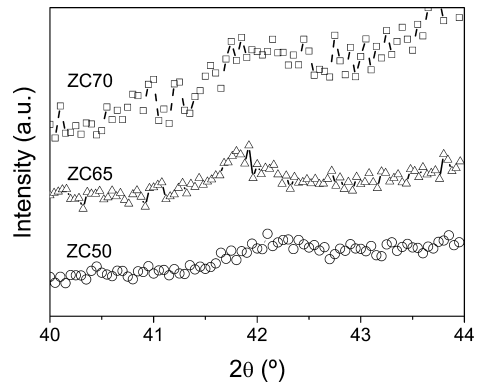

Figure 3. Room-temperature SR-XPD patterns in the vicinity of the (112) peak for nanostructured ZC50, ZC65, and ZC70 solid solutions.

clearly shows the (112) reflection measured by means of SR-XPD for ZC50, ZC65, and ZC70. As explained above, this feature is related to oxygen atoms displacement along the c axis (that characterizes the tetragonal phase) and was used in the calculation of the cation−oxygen distance, $d_{\text{cation−Oi}}$. Although oxygen atoms exhibit a small scattering cross section to X-rays, the brilliance of synchrotron sources makes it possible to resolve this low intensity reflection from background noise using an appropriate longer counting time.[11] From Figures 2 and 3, it is possible to conclude that ZC50 nanopowder exhibits at room temperature the t' form of the tetragonal phase, whereas ZC65 and ZC70 can be ascribed to the t'' form.

Rietveld refinement was performed over the SR-XPD patterns collected at room temperature. Table 1 shows the more relevant parameters of the refinements. In the case of ZC90, the c phase was assumed. From these results, together with information obtained from the evolution of the (112) reflection, it is possible to determine the correct space group for the crystal structure, indicated in the last column of Table 1.

In order to study the phase evolution of ZC50 and ZC65 as a function of temperature, scans of the 2θ = 68−75° range were performed. Figure 4a corresponds to ZC50 and shows between 600 and 800 °C a small shift to lower angles of the (400)−

dx.doi.org/10.1021/jp502457w | J. Phys. Chem. C 2014, 118, 11445−11453

Table 1. Selected Parameters of Rietveld Refinement of ZC Patterns Collected at RT[a]

sample	a (Å)	c (Å)	c/a	R_p	R_{wp}	R_e	χ^2	z(O)	space group
ZC50	5.2620(3)	5.2858(4)	1.0045(1)	5.2	5.6	3.9	2.0	0.230(2)	$P4_2/nmc$
ZC65	5.3084(1)	5.3190(2)	1.0020(1)	4.6	4.4	3.1	2.0	0.233(2)	$P4_2/nmc$
ZC70	5.3292(1)		1	4.5	4.4	2.1	4.6	0.236(2)	$P4_2/nmc$
ZC90	5.3851(1)		1	5.8	5.8	2.0	8.7	0.25*	$Fm\bar{3}m$

[a] z(O) obtained from eq 1, except (*): theoretical.

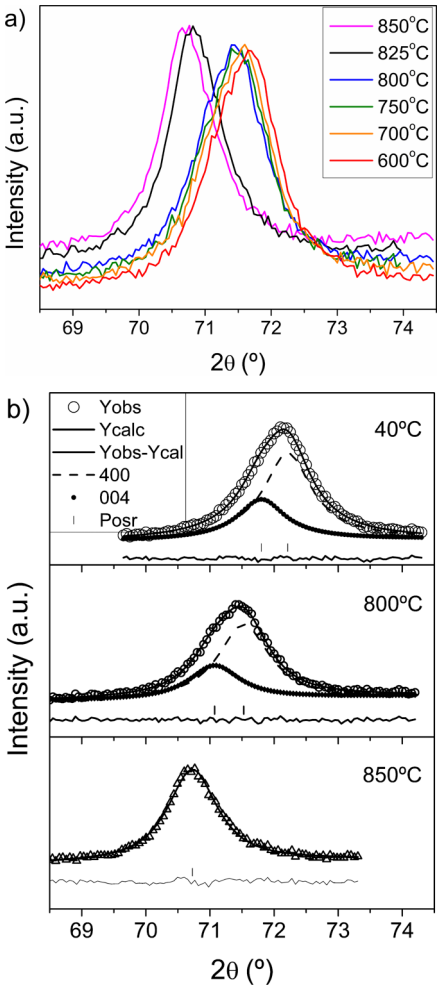

Figure 4. High-temperature SR-XPD patterns in the vicinity of the (004) and (400) peaks for nanostructured ZC50 solid solution: (a) Evolution of these peaks at different temperatures and (b) Rietveld fittings at 40, 800, and 850 °C.

(004) peaks' position, due to the thermal expansion, but between 800 and 825 °C, a jump in the peak position is observed. Analyzing the peak shape, it can be observed, between room temperature and 800 °C, the typical (004)−(400) splitting of the t' mentioned before. On the other hand, at 850 °C, the peak is symmetrical, indicating that the t'' form or c phase is present, in accordance with previous work.[12] Figure 4b shows the analysis of the data collected at 40, 800, and 850 °C. For XRD data collected at 40 °C, it is necessary to employ two pseudo-Voigt peak functions to achieve a good quality of fit. The peak function associated with the (004) reflection has half of the area of the second peak, located at higher angles. This is because the latter is associated with two reflections: the (400) and the (040). Something similar occurs at 800 °C. For XRD data collected at 850 °C, only one pseudo-Voigt function is needed to correctly fit the experimental peak and indicates that $c = a$.

Figure 5 shows the evolution of the (112) peak with temperature in ZC50. Between 40 and 800 °C, the (112) peak

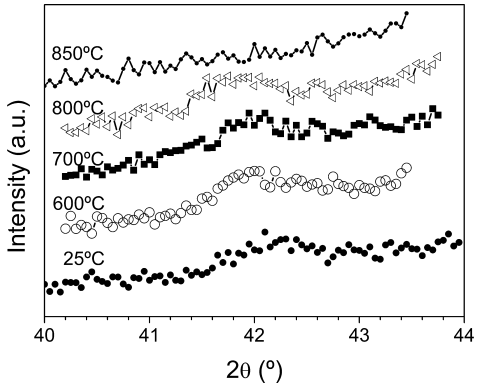

Figure 5. High-temperature SR-XPD data close to the (112) peak for the nanostructured ZC50 solid solution collected at different temperatures.

is clearly seen, but at 850 °C, this reflection is not observed. This is in accordance with the jump observed following the evolution with temperature of the (400)−(004) reflections and indicates that ZC50 nanopowder undergoes a first-order phase transition $t'-c$ between 800 and 825 °C, although a two-step transition, $t'-t''$ and $t''-c$, is expected. This fact may be due to the temperature step used in the experiment.

Rietveld refinement of the SR-XPD pattern of ZC65 nanopowder at room temperature pointed out a small asymmetry in the peak near $2\theta = 71°$, indicating that the axial ratio is $c/a > 1$ (t' form). However, between 600 and 800 °C, this peak is symmetrical, and so $c/a = 1$ (Figure 6). Nevertheless, the reflection (112) can be seen in the range of 40−800 °C (Figure 7), showing that the t'' form is present in this interval.

Table 2 shows lattice parameters and reliability factors of the Rietveld refinement performed over ZC50 and ZC65 SR-XPD patterns collected at different temperatures. In the case of ZC65, it is also possible to see the evolution of the z(O) coordinate as a function of temperature. Calculations show that z(O) approaches the 0.25 value with increasing temperature, which corresponds to the position of O atoms in the ideal fluorite structure.

Figure 8 shows cation−O distances as a function of temperature. $d_{\text{cation}-Oi}$ was calculated from the integrated intensities of (111) and (112) reflections (corresponding to SR-XPD patterns) using eq 1 and neglecting average temperature factors.[15] There it can be seen that, as the temperature increases, $d_{\text{cation}-O1}$ and $d_{\text{cation}-O2}$ approach the $d_{\text{cation}-O}$ distance in the c phase, also included in this figure and

dx.doi.org/10.1021/jp502457w | J. Phys. Chem. C 2014, 118, 11445−11453

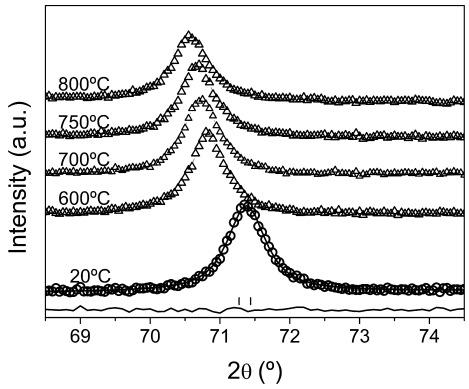

Figure 6. High-temperature SR-XPD patterns close to the (004) and (400) peaks for nanostructured ZC65 solid solution at different temperatures.

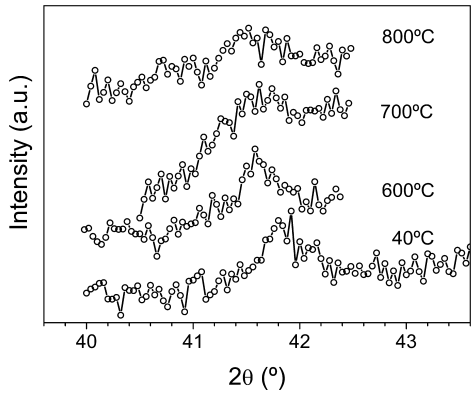

Figure 7. High-temperature SR-XPD data close to the (112) peak for the nanostructured ZC65 solid solution collected at different temperatures.

calculated from the (400) reflection and the relation $a = 2\lambda/\sin\theta_{(400)}$.

These results are in apparent contradiction to those reported by Yashima et al. on nanocrystalline, compositionally homogeneous $Ce_{0.5}Zr_{0.5}O_2$.[27] The study, performed using neutron diffraction, showed neither a jump of (400−004) peaks position nor a (112) peak intensity decrease as a function of temperature raising in the 20−900 °C interval, demonstrating that no phase transition occurs. Nevertheless, that sample was synthesized by a different chemical method, namely, the polymerized complex method. It is well-known that synthesis methods have a great influence on the crystal structure and morphology, leading to powders that, though of the same composition, exhibit qualitative different structural properties.[28]

Fittings of the Fourier transforms (FT) of EXAFS signals were performed taking SR-XRD distances $d_{cation-Oi}$ as initial values using the appropriate crystallographic models, according

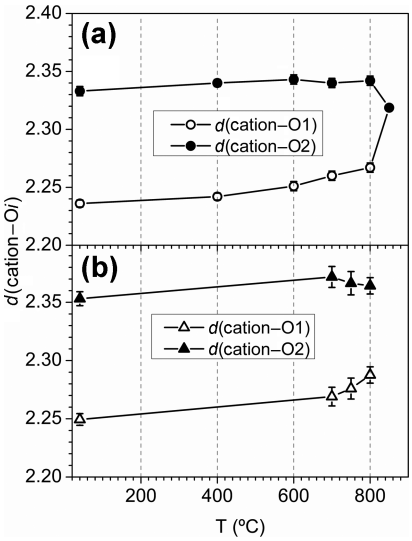

Figure 8. Cation−O distances ($d_{cation-Oi}$) of nanostructured (a) ZC50 and (b) ZC65 solid solutions calculated from high-temperature SR-XPD data employing the integrated intensities of (111) and (112) reflections (eq 1).

to the observed phase by means of SR-XPD analyses. Nevertheless, these models did not fit the experimental FT. Using the 4 + 4 model, it was possible to achieve fits of good quality (see Tables 3 and 6). The relatively high value of the σ^2 parameter obtained for the second subsphere of the first coordination shell of Zr atom suggests the presence of a distortion in the O sublattice that modifies the expected local order of Zr in ZC50. One possible interpretation of this result is that the second subsphere of nearest-neighbor (NN) oxygen atoms is split into two subspheres with two atoms in each one, as proposed in a previous work for pure ZrO_2.[29] In Figure 9a,b, a schematic plot of this explanation is exhibited. For this reason, the 4 + 2 + 2 model was analyzed, achieving fits with similar quality in the whole temperature range (see Tables 4 and 7).

The longer XPD $d_{cation-O1}$ = 2.236 Å distance compared to EXAFS R_{Zr-O1} = 2.14 Å can be explained by taking into account that XPD analysis provides information about the average cation−O distance. In this case, $d_{cation-O1}$ is the average between d_{Zr-O} and d_{Ce-O}, where $d_{Ce-O} > d_{Zr-O}$, because of the longer atomic radius of Ce^{4+} compared to that of Zr^{4+} (0.97 Å for Ce^{4+} and 0.84 Å for Zr^{4+}).[15,30] This fact also explains the increase of $d_{cation-Oi}$ with increasing loading of Ce content in zirconia−ceria solid solutions, as shown previously in Figure 2.

As mentioned before, this local order model for the Zr in ZC50 can be interpreted in terms of distortions of the O sublattice. Both second and third subspheres may be the result of an extra displacement of O atoms along the (110) direction in the pseudocubic unit cell (see Figure 10), as it has been

Table 2. Rietveld Refinement Parameters of Patterns of ZC Collected at HT[a]

sample	T (°C)	a (Å)	c (Å)	c/a	R_p	R_{wp}	R_e	χ^2	z(O)	space group
ZC50	850	5.3514(1)		1	8.3	8.1	4.3	3.6	0.25*	$Fm\bar{3}m$
ZC65	600	5.3507(7)		1	5.1	5.0	2.7	3.3	0.231(3)	$P4_2/nmc$
ZC65	700	5.3564(2)		1	4.8	4.6	2.8	2.6	0.233(2)	$P4_2/nmc$
ZC65	750	5.3580(2)		1	5.3	5.1	2.9	3.2	0.235(2)	$P4_2/nmc$
ZC65	800	5.3701(5)		1	5.6	5.2	2.7	3.7	0.238(1)	$P4_2/nmc$

[a]ZC50 at 850 °C; ZC65 at 600, 700, 750, and 800 °C. z(O) obtained from eq 1, except (*): theoretical.

dx.doi.org/10.1021/jp502457w | J. Phys. Chem. C 2014, 118, 11445−11453

Table 3. EXAFS 4 + 4 Model for ZC50-GCNoEG[a]

model	shell	subshell	N	R (Å)	σ^2 (Å^2)	ΔE_0 (eV)
4 + 4	1	1	4	v	$\sigma_{11} \neq \sigma_{12}$ (v)	$-2 < \Delta E_{01} < 2$ (v)
		2	4	v		$\Delta E_{02} = \Delta E_{01}$
	2	1	2Zr + 2Ce	v	$\sigma_{21} = \sigma_{22}$ (v)	$\Delta E_{03} = \Delta E_{01}$
		2	4Zr + 4Ce	v		$\Delta E_{04} = \Delta E_{01}$

[a]N: coordination number; R: Zr−O distance; σ: Debye−Waller factor; ΔE_0: energy shift correction to the absorption energy edge E_0; v: variable.

Table 4. EXAFS 4 + 2 + 2 Model[a]

shell	subshell	N	R (Å)	σ^2 (Å^2)	ΔE_0 (eV)
1	1	4	v	$\sigma_{11} = \sigma_{12} = \sigma_{13}$ (v)	$-2 < \Delta E_{01} < 2$ (v)
	2	2	v		$\Delta E_{02} = \Delta E_{01}$
	3	2	v		$\Delta E_{03} = \Delta E_{01}$
2	1	2Zr + 2Ce	v	$\sigma_{21} = \sigma_{22}$ (v)	$\Delta E_{04} = \Delta E_{01}$
	2	4Zr + 4Ce	v		$\Delta E_{05} = \Delta E_{01}$

[a]N: coordination number; R: Zr−O distance; v: variable.

Table 5. EXAFS 4 + 3 + 1 Model for ZC65-GCNoEG[a]

shell	subshell	N	R (Å)	σ^2 (Å^2)	ΔE_0 (eV)
1	1	4	v	$\sigma_{11} = \sigma_{12} = \sigma_{13}$ (v)	$-2 < \Delta E_{01} < 2$ (v)
	2	3	v		$\Delta E_{02} = \Delta E_{01}$
	3	1	v		$\Delta E_{03} = \Delta E_{01}$
2	1	nCe	v	$\sigma_{21} = \sigma_{22}$ (v)	$\Delta E_{04} = \Delta E_{01}$
	2	4.2Zr + (7.8 − n)Ce	v		$\Delta E_{05} = \Delta E_{01}$

[a]N: coordination number; R: Zr−O distance; v: variable; n: variable factor for the coordination number of the second sphere of Ce.

Table 6. EXAFS Fitting Results for ZC50 Employing the 4 + 4 Model[a]

			R (Å)				σ^2 (×10^4 Å^2)			
shell	subshell	N	20	200	400	600	20	200	400	600
1 (O)	1	4	2.14(2)	2.12(2)	2.12(2)	2.18(2)	32(13)	55(15)	62(10)	81(10)
	2	4	2.30(4)	2.28(4)	2.29(2)	2.39(7)	78(35)	92(35)	93(20)	275(134)
2 (Zr/Ce)		2 Zr	3.31(6)	3.38(6)	3.35(3)	3.32(5)	82(33)	105(39)	111(24)	109(60)
		2 Ce	3.31(6)	3.38(6)	3.35(3)	3.32(5)				
		4 Zr	3.64(5)	3.65(4)	3.63(2)	3.63(3)				
		4 Ce	3.70(3)	3.71(4)	3.70(3)	3.66(9)				

[a]N: coordination number; R: Zr−O distance. $\Delta E_0 = -2$ eV. Goodness of fit (r-factor) was between 0.02 and 0.04.

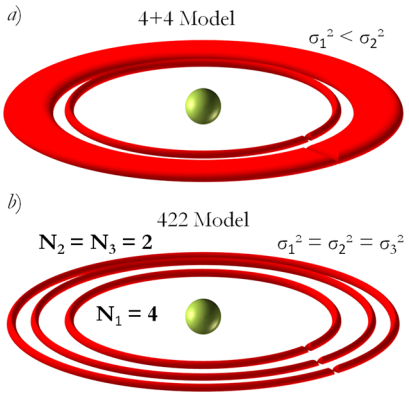

Figure 9. Schematic representations of (a) 4 + 4 model and (b) 4 + 2 + 2 model.

proposed to occur in pure ZrO_2.[29] This displacement maintains four O atoms in the first subshell, but splits the second into two subshells with two O atoms each. Simple calculations show that, if the O atoms are randomly displaced (in one way or the opposite) along the (110) direction, in an amount of $\delta(110) \approx$ 0.07 Å, the Zr−O distances determined by EXAFS are obtained, but because of the random displacement, only two O subshells can be seen by XPD analyses, with the d_{Zr-O2} distance as the average of R'_{Zr-O2} and R'_{Zr-O3}. This model fits satisfactorily in the whole temperature range. At 600 °C, a displacement of $\delta(110) \approx 0.20$ Å can account for the six O atoms at 2.20 Å and two at 2.45 Å.

The 4 + 2 + 2 model failed when used for fitting the FT of the EXAFS signal corresponding to ZC65, as well as the crystallographic t- and c-models.

After exploring different possibilities, a 4 + 3 + 1 model turned out to be the one that achieved good quality of fit for ZC65, ZC70, and ZC90 FTs (see Tables 8, 9 and 10). Nevertheless, the interpretation of this model in terms of a distortion of the expected local order for the corresponding phases remained unclear. Taking into account that the EXAFS signal contains the contribution of all the Zr atoms in the illuminated region, it is, in fact, an average of the different local orders of Zr in ZC samples. In this way, the 4 + 3 + 1 model can be thought of as the superposition of the contribution of two different local orders: on one hand, the one represented by the standard t-model (4 + 4) and, on the other hand, the 4 + 2

dx.doi.org/10.1021/jp502457w | J. Phys. Chem. C 2014, 118, 11445−11453

Table 7. EXAFS Fitting Results for ZC50 Employing the 4 + 2 + 2 Model[a]

			R (Å)				σ^2 ($\times 10^4$ Å^2)			
shell	subshell	N	20	200	400	600	20	200	400	600
1 (O)	1	4	2.14(2)	2.11(2)	2.12(2)	2.20(2)				
	2	2	2.23(4)	2.23(4)	2.24(2)	2.20(7)	33(21)	55(16)	62(10)	106(10)
	3	2	2.35(4)	2.33(4)	2.34(2)	2.45(3)				
2 (Zr/Ce)		2 Zr	3.31(6)	3.34(6)	3.34(3)	3.34(5)	103(43)	104(31)	116(15)	125(29)
		2 Ce	3.31(6)	3.34(6)	3.34(3)	3.34(5)				
		4 Zr	3.65(5)	3.63(5)	3.63(2)	3.62(3)				
		4 Ce	3.74(9)	3.71(3)	3.70(2)	3.66(3)				

[a]N: coordination number; R: Zr−O distance. ΔE_0 = −2 eV. r-factor = (0.02−0.04).

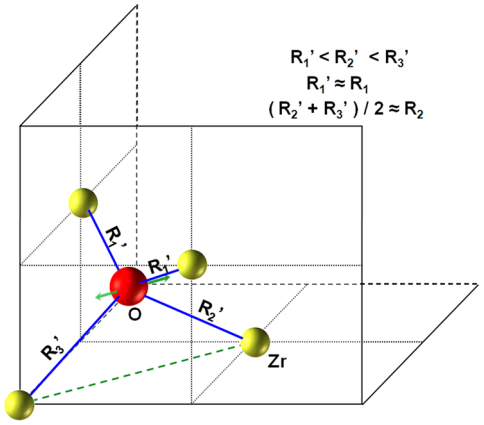

Figure 10. Schematic representation of displacement of the O atoms along the (110) direction in the pseudocubic unit cell.

+ 2 model, with the restrain that the first and second R_{Zr-O1} and R_{Zr-O2} distances of the t-model to be equal to R'_{Zr-O1} and R'_{Zr-O2} of the 4 + 2 + 2 model (see Figure 11). In this picture, half of the Zr atoms have a local order that can be described by the (more ordered) t-model and the other half by the 4 + 2 + 2 model. Explicitly, the local order of Zr in ZC65, ZC70, and ZC90 is described by the 4 + 3 + 1 model, whereas the one corresponding to the ZC50 sample can be described entirely by the 4 + 2 + 2 model.

At first glance, it seems striking that the relative weight of both local orders of Zr remains unchanged upon Ce loading from 65 to 90 mol % CeO_2, even when the ZrO_2−CeO_2 system undergoes a phase transition from the t'' form to the c phase near the 85 mol % CeO_2, as stated by SR-XPD analyses. Nevertheless, it has to be taken into account that the amount of Zr is decreasing, and as a consequence, the displacement along the c axis of the O atoms is more difficult to detect by XPD. This fact also suggests that Zr retains its local order almost unchanged in the range of 50−90 mol % CeO_2.

Table 9. EXAFS Fitting Results for ZC70 Employing the 4 + 3 + 1 Model[a]

shell	subshell	N	R (Å)	σ^2 ($\times 10^4$ Å^2)
1 (O)	1	4	2.16(1)	33(10)
	2	3	2.31(2)	
	3	1	2.45(4)	
2 (Zr/Ce)	1	1.9(4) (Ce)	3.47(1)	71(7)
	2	3.6(7) (Zr)	3.78(2)	
	2	6.5(7) (Ce)		

[a]N: coordination number; R: Zr−O distance. ΔE_0 = −2 eV. r-factor = 0.04.

Table 10. EXAFS Fitting Results for ZC90 Employing the 4 + 3 + 1 Model[a]

shell	subshell	N	R (Å)	σ^2 ($\times 10^4$ Å^2)
1 (O)	1	4	2.18(1)	35(15)
	2	3	2.34(2)	
	3	1	2.61(4)	
2 (Zr/Ce)	1	1.6(6) (Ce)	3.51(2)	73(7)
	2	1.2(2) (Zr)	3.79(2)	
	2	9.2(6) (Ce)		

[a]N: coordination number; R: Zr−O distance. ΔE_0 = −2 eV. r-factor = 0.04.

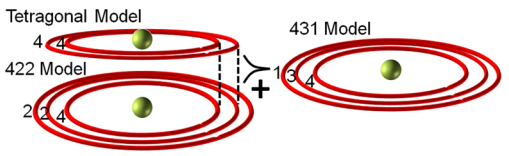

Figure 11. Schematic representation of 4 + 3 + 1 model.

Fitting results of the ZC65 FT show that, with increasing temperature, the local order of Zr evolves to the one exhibited by Zr in ZC90 at room temperature, whereas, at room

Table 8. EXAFS Fitting Results for ZC65 Employing the 4 + 3 + 1 Model[a]

			R (Å)			σ^2 ($\times 10^4$ Å^2)		
shell	subshell	N	20	400	600	20	400	600
1 (O)	1	4	2.14(2)	2.15(1)	2.14(1)			
	2	3	2.28(3)	2.34(1)	2.33(2)	39(11)	52(4)	66(6)
	3	1	2.40(4)	2.60(2)	2.61(2)			
2 (Zr/Ce)	1	2.0 Ce	3.47(1)	3.45(1)	3.47(2)	63(8)	121(8)	142(14)
	2	4.2 Zr	3.78(2)	3.77(2)	3.77(2)			
	3	5.8 Ce	3.78(2)	3.77(2)	3.77(2)			

[a]N: coordination number; R: Zr−O distance. ΔE_0 = −2 eV. r-factor = (0.02−0.04).

dx.doi.org/10.1021/jp502457w | J. Phys. Chem. C 2014, 118, 11445−11453

temperature, it is more similar to that corresponding to ZC70 (see *R* parameter in Tables 8, 9, and 10).

The second coordination sphere of Ce^{4+} and Zr^{4+}cations in ZC50 exhibits the expected splitting of the *t*′ form, with cations of both elements mixed uniformly in the whole range of temperatures. In the case of the second subshell, Zr^{4+} cations are placed at a shorter distance of the central Zr atom than Ce^{4+} cations. In the cases of ZC65, ZC70, and even ZC90, the splitting still exists, but the first subshell is composed of only Ce^{4+} cations, whereas the second contains a mixture of both located at the same distance. The responsible distortion in the cation lattice in terms of the long-range order of XPD remains unsolved. Probably, ab initio calculations related to the structure and electronic properties of these materials, mostly involving the stability of cation positions, can shine a light on this issue.

CONCLUSIONS

In this work, the local order of the Zr atom in ZrO_2−CeO_2 was studied by means of the EXAFS technique for different compositions and as a function of temperature in the range of 40−600 °C. On the basis of electroneutrality of the unit cell and on previous works, in which it was determined that almost all Ce is in the +4 oxidation state in these samples, the existence of no vacancies in the oxygen sublattice was assumed. Local order models, which can be interpreted in terms of distortions of the accepted crystal structure (determined here by SR-XPD analyses), were considered.

The results suggested the existence of distortions in the oxygen sublattice, which can be accounted for by displacements of the oxygen atoms along the (110) direction of the pseudofluorite unit cell, as it has been proposed to occur in pure ZrO_2. Nevertheless, by means of XPD, it is not possible to see this effect because of the random nature of these displacements.

AUTHOR INFORMATION

Corresponding Author

*E-mail: lacuna@citedef.gob.ar. Phone: +5411 4709 8158.

Notes

The authors declare no competing financial interest.

ACKNOWLEDGMENTS

This work was supported by the LNLS (Brazilian Synchrotron Light Laboratory, Brazil) under research proposals XAFS1-4700, XAFS1-7225, XPD-6674 and XPD-7083, ANPCyT, CONICET and MinCyT-CAPES cooperation agreement.

REFERENCES

(1) Kaspar, J.; Fornasiero, P. *Catalysis by Ceria and Related Materials*; Trovarelli, A., Ed.; Imperial College Press: London, 2002; Chapter 6.

(2) Di Monte, R.; Kaspar, J. Nanostructured CeO_2−ZrO_2 Mixed Oxides. *J. Mater. Chem.* **2005**, *15*, 633−648.

(3) Yashima, M.; Ohtake, K.; Arashi, H.; Kakihana, M.; Yoshimura, M. Determination of Cubic-Tetragonal Phase Boundary in $Zr_{1-X}Y_XO_{2-X/2}$ Solid Solutions by Raman Spectroscopy. *J. Appl. Phys.* **1993**, *74*, 7603−7606.

(4) Yashima, M.; Sasaki, S.; Kakihana, M.; Yamaguchi, Y.; Arashi, H.; Yoshimura, M. Oxygen-Induced Structural Change of the Tetragonal Phase around the Tetragonal−Cubic Phase Boundary in ZrO_2−$YO_{1.5}$ Solid Solutions. *Acta Crystallogr., Sect. B* **1994**, *50*, 663−672.

(5) Yashima, M.; Kakihana, M.; Yoshimura, M. Metastable-Stable Phase Diagrams in the Zirconia-Containing Systems Utilized in Solid-Oxide Fuel Cell Application. *Solid State Ionics* **1996**, *86*, 1131−1149.

(6) Yashima, M.; Ohtake, K.; Kakihana, M.; Arashi, H.; Yoshimura, M. Determination of Tetragonal-Cubic Phase Boundary of $Zr_{1-X}R_XO_{2-X2}$ (R = Nd, Sm, Y, Er and Yb) by Raman Scattering. *J. Phys. Chem. Solids* **1996**, *57*, 17−24.

(7) Yashima, M.; Kakihana, M.; Ishii, K.; Ikuma, Y.; Yoshimura, M. Synthesis of Metastable Tetragonal (t′) Zirconia-Calcia Solid Solution by Pyrolysis of Organic Precursors and Coprecipitation Route. *J. Mater. Res.* **1996**, *11*, 1410−1420.

(8) Yashima, M.; Sasaki, S.; Yamaguchi, Y.; Kakihana, M.; Yoshimura, M.; Mori, T. Internal Distortion in ZrO_2−CeO_2Solid Solutions: Neutron and High-Resolution Synchrotron X-ray Diffraction Study. *Appl. Phys. Lett.* **1998**, *72*, 182−185.

(9) Yashima, M.; Arashi, H.; Kakihana, M.; Yoshimura, M. Raman Scattering Study of Cubic−Tetragonal Phase Transition in $Zr_{1-x}Ce_xO_2$ Solid Solution. *J. Am. Ceram. Soc.* **1994**, *77*, 1067−1071.

(10) Lamas, D. G.; Lascalea, G. E.; Juárez, R. E.; Djurado, E.; Pérez, L.; Walsöe de Reca, N. E. Metastable Forms of the Tetragonal Phase in Compositionally Homogeneous, Nanocrystalline Zirconia−Ceria Powders Synthesised by Gel-Combustion. *J. Mater. Chem.* **2003**, *13*, 904−910.

(11) Lamas, D. G.; Fuentes, R. O.; Fábregas, I. O.; Fernández de Rapp, M. E.; Lascalea, G. E.; Casanova, J. R.; Walsöe de Reca, N. E.; Craievich, A. F. Synchrotron X-Ray Diffraction Study of the Tetragonal-Cubic Phase Boundary of Nanocrystalline ZrO_2-CeO_2 Synthesised by a Gel-Combustion Process. *J. Appl. Crystallogr.* **2005**, *38*, 867−873.

(12) Acuña, L. M.; Fuentes, R. O.; Lamas, D. G.; Fábregas, I. O.; Walsöe de Reca, N. E. High-Temperature XPD Study of the Tetragonal-Cubic Phase Transition in Nanocrystalline, Compositionally Homogeneous ZrO_2-CeO_2 Solid Solutions. *Powder Diffr.* **2008**, *23*, S70−S74.

(13) Fuentes, R. O.; Baker, R. T. Synthesis of Nanocrystalline ZrO_2-CeO_2 Solid Solutions by a Citrate Complexation Route: a Thermochemical and Structural Study. *J. Phys. Chem. C* **2009**, *113*, 914−924.

(14) Fuentes, R. O.; Acuña, L. M.; Zimicz, M. G.; Lamas, D. G.; Sacanell, J. G.; Leyva, A. G.; Baker, R. T. Formation and Structural Properties of Ce-Zr Mixed Oxide Nanotubes. *Chem. Mater.* **2008**, *20*, 7356−7363.

(15) Fábregas, I. O.; Fuentes, R. O.; Lamas, D. G.; Fernández de Rapp, M. E.; Walsöe de Reca, N. E.; Fantini, M. C. A.; Craievich, A. F.; Prado, R. J.; Millen, R. P.; Temperini, M. L. A. Local Structure of the Metal-Oxygen Bond in Compositionally Homogeneous, Nanocrystalline Zirconia-Ceria Solid Solutions Synthesized by a Gel-Combustion Process. *J. Phys.: Condens. Matter* **2006**, *18*, 7863−7881.

(16) Vlaic, G.; Fornasiero, P.; Geremia, S.; Kaspar, J.; Graziani, M. Relationship between the Zirconia-Promoted Reduction in the Rh-Loaded $Ce_{0.5}Zr_{0.5}O_2$Mixed Oxide and the Zr−O Local Structure. *J. Catal.* **1997**, *168*, 386−392.

(17) Meriani, S.; Spinolo, G. Powder Data for Metastable $Zr_xCe_{1-x}O_2$ (x = 0.84 to 0.40) Solid Solutions with Tetragonal Symmetry. *Powder Diffr.* **1987**, *2*, 255−257.

(18) Lemaux, S.; Bensaddik, A.; van der Eerden, A. M. J.; Bitter, J. H.; Koningsberger, D. C. Understanding of Enhanced Oxygen Storage Capacity in $Ce_{0.5}Zr_{0.5}O_2$: The Presence of an Anharmonic Pair Distribution Function in the Zr−O2 Subshell as Analyzed by XAFS Spectroscopy. *J. Phys. Chem. B* **2001**, *105*, 4810−4815.

(19) Li, P.; Chen, I.-W.; Penner-Hahn, J. E. Effect of Dopants on Zirconia Stabilization-An X-ray Absorption Study: II, Tetravalent Dopants. *J. Am. Ceram. Soc.* **1994**, *77*, 1281−1288.

(20) Mastelaro, V. R.; Briois, V.; de Souza, D. P. F.; Silva, C. L. Structural Studies of a ZrO_2−CeO_2 Doped System. *J. Eur. Ceram. Soc.* **2003**, *23*, 273−282.

(21) Ferreira, F. F.; Granado, E.; Carvalho, W., Jr.; Kycia, S. W.; Bruno, D.; Droppa, R., Jr. X-ray Powder Diffraction Beamline at D10B

of LNLS: Application to the Ba_2FeReO_6 Double Perovskite. *J. Synchrotron Radiat.* **2006**, *13*, 46−53.
(22) Tolentino, H.; Cezar, J. C.; Cruz, D. Z.; Compagnon-Cailhol, V.; Tamura, E.; Martins Alves, M. C. Commissioning and First Results of the LNLS XAFS Beamline. *J. Synchrotron Radiat.* **1998**, *5*, 521−523.
(23) Ressler, T. WinXAS: A Program for X-ray Absorption Spectroscopy Data Analysis under MS-Windows. *J. Synchrotron Radiat.* **1998**, *5*, 118−122.
(24) Ravel, B. ATOMS: Crystallography for the X-ray Absorption Spectroscopist. *J. Synchroton Radiat.* **2001**, *8*, 314−316.
(25) Ankudinov, A. L.; Ravel, B.; Rehr, J. J.; Conradson, S. D. Real-Space Multiple-Scattering Calculation and Interpretation of X-ray-Absorption Near-Edge Structure. *Phys. Rev. B* **1998**, *58*, 7565−7576.
(26) Newville, M.; Ravel, B.; Haskel, D.; Rehr, J. J.; Stern, A.; Yacoby, Y. Analysis of Multiple-Scattering XAFS Data Using Theoretical Standards. *Physica B* **1995**, *208−209*, 154−156.
(27) Yashima, M.; Sekikawa, T.; Sato, D.; Nakano, H.; Omoto, K. Crystal Structure and Oxide-Ion Diffusion of Nanocrystalline, Compositionally Homogeneous Ceria−Zirconia $Ce_{0.5}Zr_{0.5}O_2$ up to 1176 K. *Cryst. Growth Des.* **2013**, *13*, 829−837.
(28) Alifanti, M.; Baps, B.; Blangenois, N.; Naud, J.; Grange, P.; Delmon, B. Characterization of CeO_2−ZrO_2 Mixed Oxides. Comparison of the Citrate and Sol−Gel Preparation Methods. *Chem. Mater.* **2003**, *15*, 395−403.
(29) Acuña, L. M.; Lamas, D. G.; Fuentes, R. O.; Fábregas, I. O.; Fantini, M. C. A.; Craievich, A. F.; Prado, R. J. Local Atomic Structure in Tetragonal ZrO_2Nanopowders. *J. Appl. Crystallogr.* **2010**, *43*, 227−236.
(30) Shannon, R. D. Revised Effective Ionic Radii and Systematic Studies of Interatomic Distances in Halides and Chalcogenides. *Acta Crystallogr., Sect. A* **1976**, *32*, 751−767.